










SDSS-IV MaNGA: Evidence for Enriched Accretion onto Satellite Galaxies in Dense Environments

Adam L. Schaefer¹, Christy Tremonti¹, Zachary Pace¹ , Francesco Belfiore² , Maria Argudo-Fernandez³,
Matthew A. Bershadsky^{1,4} , Niv Drory⁵ , Amy Jones⁶, Roberto Maiolino⁷, David Stark⁸ , David Wake⁹ , and Renbin Yan¹⁰ 

¹Department of Astronomy, University of Wisconsin–Madison, 475 N. Charter St., Madison, WI 53703, USA

²European Southern Observatory, Karl-Schwarzschild-Str. 2, Garching bei München, D-85748, Germany

³Instituto de Física, Pontificia Universidad Católica de Valparaíso, Casilla 4059, Valparaíso, Chile

⁴South African Astronomical Observatory, P.O. Box 9, Observatory 7935, Cape Town, South Africa

⁵McDonald Observatory, The University of Texas at Austin, 1 University Station, Austin, TX 78712, USA

⁶University of Alabama, Department of Physics and Astronomy, Tuscaloosa, AL 35487, USA

⁷University of Cambridge, Cavendish Laboratory, 19 J.J. Thomson Avenue, Cambridge CB3 0HE, UK

⁸Kavli IPMU (WPI), UTIAS, The University of Tokyo, Kashiwa, Chiba 277-8583, Japan

⁹University of North Carolina at Asheville, Department of Physics, 1 University Heights, Asheville, NC 28804, USA

¹⁰Department of Physics and Astronomy, University of Kentucky, 505 Rose St., Lexington, KY 40506, USA

Received 2019 July 15; revised 2019 August 28; accepted 2019 September 9; published 2019 October 22

Abstract

We investigate the environmental dependence of the local gas-phase metallicity in a sample of star-forming galaxies from the MaNGA survey. Satellite galaxies with stellar masses in the range $9 < \log(M_*/M_\odot) < 10$ are found to be ~ 0.05 dex higher in metallicity than centrals of similar stellar mass. Within the low-mass satellite population, we find that the interstellar medium (ISM) metallicity depends most strongly on the stellar mass of the galaxy that is central to the halo, though there is no obvious difference in the metallicity gradients. At fixed total stellar mass, the satellites of high-mass ($M_* > 10^{10.5} M_\odot$) centrals are ~ 0.1 dex more metal-rich than the satellites of low-mass ($M_* < 10^{10} M_\odot$) centrals, controlling for local stellar mass surface density and gas fraction. Fitting a gas regulator model to the spaxel data, we are able to account for variations in the local gas fraction, stellar mass surface density, and local escape velocity–dependent outflows. We find that the best explanation for the metallicity differences is the variation in the average metallicity of accreted gas between different environments that depends on the stellar mass of the dominant galaxies in each halo. This is interpreted as evidence for the exchange of enriched gas between galaxies in dense environments that is predicted by recent simulations.

Unified Astronomy Thesaurus concepts: [Metallicity \(1031\)](#); [Intergalactic abundances \(2003\)](#); [Galactic abundances \(2002\)](#); [Scaling relations \(2031\)](#); [Intergalactic gas \(812\)](#); [Galaxy accretion \(575\)](#); [Spectroscopy \(1558\)](#); [Galaxy environments \(2029\)](#); [Galaxy evolution \(594\)](#)

1. Introduction

Star formation in galaxies is maintained through the continued accretion of gas from the intergalactic medium. In turn, the chemical properties of the interstellar medium (ISM) within galaxies are modulated by the processes of stellar evolution and feedback and the abundances of elements within the accreted material. Studies of large samples of galaxies have demonstrated correlations between the gas-phase oxygen abundance in the ISM of galaxies and the total stellar mass (Tremonti et al. 2004), star formation rate (Mannucci et al. 2010), and gravitational potential (D’Eugenio et al. 2018).

These empirical correlations between global galaxy properties and metallicity hint at three processes that can influence the metal content of galaxies. With the buildup of stellar mass through star formation, heavy elements are synthesized in the cores of stars and deposited in the ISM through stellar winds and the terminal phases of the stellar life cycle (see, e.g., Maiolino & Mannucci 2019). Assuming that this enriched material mixes efficiently into the ISM, the metallicity will then depend on the metal yield from the stars and the amount of gas into which these metals are dispersed. In other words, the metallicity depends on the degree to which the nucleosynthetic products of stellar evolution are diluted in the ISM (e.g., Larson 1972; Moran et al. 2012; Bothwell et al. 2013). Meanwhile, winds driven by the energy or momentum injected

into the ISM through stellar feedback have been shown to remove enriched material from galaxies (Heckman et al. 1990). The magnitude of the effect of metal loss from galaxies due to outflows on setting their metallicity is not known precisely. This is determined by both the mass-loading factor, λ , which quantifies the total mass lost for a given rate of star formation, and the metal-loading factor, which describes the metal content of the outflow. Recent work by Chisholm et al. (2018) found that the metallicity of outflowing material is independent of the stellar mass of a galaxy and therefore of the ISM metallicity. However, it is often assumed that the expelled gas has the same metallicity as the ISM (Erb 2008; Finlator & Davé 2008).

The trade-off between these different galactic processes has been captured by a number of different attempts to model the chemical evolution of galaxies (e.g., Finlator & Davé 2008; Peebles & Shankar 2011; Lilly et al. 2013). The Lilly et al. (2013) model makes the simplifying assumption that the evolution of a galaxy’s star formation and metallicity are determined almost entirely by the total gas content. Making simple assumptions about the flow of gas into and out of galaxies, these models are able to reproduce the global mass–metallicity relation, along with the star formation rate–stellar mass relation.

Given the success of analytic models in describing the global properties of galaxies, there has been a recent effort to extend the global scaling relations to kiloparsec scales within galaxies

(e.g., Rosales-Ortega et al. 2012; Barrera-Ballesteros et al. 2016; Cano-Díaz et al. 2016; Medling et al. 2018). These studies have been enabled by the introduction of large-scale spatially resolved spectroscopic surveys such as the Calar Alto Legacy Integral Field Area Survey (CALIFA; Sánchez et al. 2012), Sydney-AAO Multi-object Integral Field Spectrograph (SAMI; Croom et al. 2012; Bryant et al. 2015), and Mapping Nearby Galaxies at Apache Point Observatory (MaNGA; Bundy et al. 2015). Cano-Díaz et al. (2016) found that the gas-phase metallicity in kiloparsec-sized regions of galaxies is tightly correlated with the stellar mass surface density, Σ_* . However, Barrera-Ballesteros et al. (2016) showed that this correlation is also dependent on the total stellar mass of the galaxy. That is, at fixed Σ_* , the gas-phase metallicity is correlated with the integrated stellar mass. In direct analogy, in an argument connecting the global mass–metallicity relation to the increasing depth of the gravitational potential well in more massive galaxies, Barrera-Ballesteros et al. (2018) showed that the local metallicity also correlates with the local escape velocity. This may explain the connection of the local Σ_* –metallicity relation to the integrated stellar mass.

The existence of local scaling relations is an indicator that some kind of regulatory process is at play, and that processes occurring on local scales may be able to explain the results seen in single-fiber spectroscopic surveys (Barrera-Ballesteros et al. 2016). Indeed, work by Carton et al. (2015) and Barrera-Ballesteros et al. (2018) found that the Lilly et al. (2013) gas regulator model is able to fit the metallicity given a reasonable estimate of the local gas fraction and mass-loading factors.

The ability of gas-regulated models to achieve an equilibrium is in part determined by the rate at which gas is accreted and the metallicity of that gas. Historically, it was often assumed that the gas fueling star formation is accreted in a chemically pristine state (e.g., Larson 1972; Quirk & Tinsley 1973; Finlator & Davé 2008; Mannucci et al. 2010). However, there is mounting evidence that this is not the case (Oppenheimer et al. 2010; Rubin et al. 2012; Brook et al. 2014; Kacprzak et al. 2016; Gupta et al. 2018). While work such as that done by Peng & Maiolino (2014) relies on the inference of the properties of gas in the intergalactic medium from modeling, there is a growing body of observations that are able to directly probe the metallicity of gas outside of galaxies by measuring the absorption of background quasar light by extragalactic clouds (Lehner et al. 2013; Prochaska et al. 2017). These clouds are observed to be cool and metal-rich and are expected to be accreted onto their host galaxies in the future. Indeed, hydrodynamic simulations (Oppenheimer et al. 2010) have shown that below $z \sim 1$, the dominant source of accreted gas onto galaxies is material that was previously ejected.

In addition to internal processes such as star formation and the expulsion of gas by feedback, there are a number of ways in which the gas content of a galaxy could be diminished by external environmental processes. Starvation (Larson et al. 1980) can occur when a galaxy enters a dense environment and the acquisition of new gas is prevented. In this instance, the existing gas reservoir is consumed by star formation over several Gyr, and the metallicity of the ISM increases. Starvation can also be initiated through the heating of gases in the intergalactic medium by galactic feedback (e.g., Fielding et al. 2017) or by the shock heating of accreted material (e.g., Birnboim & Dekel 2003). Alternatively, a kinetic interaction between the ISM of a galaxy and the intergalactic medium can

result in the ram pressure stripping of gas from a galaxy (Gunn & Gott 1972). Occurring on relatively short (<100 Myr) timescales, ram pressure stripping is not expected to alter the chemical abundances in a galaxy before it is fully quenched.

Studies of the environmental effect on galaxy metallicities generally find a small but significant dependence. For example, Cooper et al. (2008) found that approximately 15% of the scatter in the mass–metallicity relation is attributable to an increase in the metallicity of galaxies in high-density environments. Observationally, there is a consensus that the environment has the largest effect on low-mass galaxies (Pasquali et al. 2012; Peng & Maiolino 2014; Wu et al. 2017). However, the interpretation of this fact is contentious. Wu et al. (2017) attributed the elevated metallicity at fixed stellar mass at greater local galaxy overdensity to a reduction in the gas accretion rate. However, Peng & Maiolino (2014) showed that even when the star formation rates of satellite galaxies in different environments are kept constant, implying no change in the total accretion rate, the metallicity offset is still evident. Their observations and modeling led them to the conclusion that satellite galaxies in dense environments must acquire more enriched gas from their surroundings.

In this paper, we make use of the broad range of galaxy environments and stellar masses covered by the MaNGA survey to explore how the local metallicity scaling relations are affected by the environment for satellite and central galaxies. With MaNGA’s wide wavelength coverage and spatial resolution, we are able to estimate local gas-phase metallicities, gas mass fractions, and escape velocities to compare the observations to a model for the gas regulation of the metallicity, and from this modeling, we infer environmental trends for the metallicity of gas inflows.

In Section 2, we present our data and analysis techniques. In Section 3 we investigate how galaxy environments change the local metallicity scaling relations, and in Section 4, we discuss our observations in the context of the Lilly et al. (2013) gas regulator model. Throughout this paper, we assume a flat Λ CDM cosmology, with $H_0 = 70 \text{ km s}^{-1} \text{ Mpc}^{-1}$, $\Omega_\Lambda = 0.7$, and $\Omega_m = 0.3$. Unless otherwise stated, we assume a Chabrier (2003) stellar initial mass function. We will make use of two oxygen abundance indicators, which each have different absolute abundance scales. The O3N2 (Pettini & Pagel 2004) assumes $12 + \log(\text{O}/\text{H})_\odot = 8.69$, and the N2S2H α indicator (Dopita et al. 2016) assumes $12 + \log(\text{O}/\text{H})_\odot = 8.77$.

2. Methods

To investigate the trends of the spatially resolved metal distribution in galaxies with environment, we make use of the eighth MaNGA product launch (MPL-8) internal data release, which is similar to the Sloan Digital Sky Survey (SDSS) DR15 (Aguado et al. 2019) but includes data from 6507 unique galaxies. In this section, we describe the data, sample selection, and methods used to perform our analysis of these data.

2.1. MaNGA Data

The MaNGA survey is the largest optical integral field spectroscopic survey of galaxies to date. Run on the 2.5 m SDSS telescope (Gunn et al. 2006) at Apache Point Observatory, the MaNGA survey aims to observe approximately 10,000 galaxies. This sample comprises primary and secondary subsamples that were selected to have approximately

flat distributions in the i -band absolute magnitude, M_i . These provide coverage of galaxies out to 1.5 and 2.5 R_e , respectively (Wake et al. 2017), and median physical resolutions of 1.37 and 2.5 kpc.

Observations of each galaxy are made with one of 17 hexagonal optical fiber hexabundles, each comprising between 19 and 127 $2''$ optical fibers, subtending between $12''$ and $32''$ on the sky. The fiber faces fill the bundle with 56% efficiency, so each target is observed with a three-point dither pattern with 15 minute exposures per pointing. This pattern of observations is repeated until a median signal-to-noise ratio (S/N) of 20 fiber $^{-1}$ pixel $^{-1}$ is achieved in the g band, which is typically 2–3 hr in total (Law et al. 2015; Yan et al. 2016). Light from each hexabundle is taken from the fibers to the BOSS spectrograph (Smee et al. 2013), where it is split by a dichroic at ~ 6000 Å into red and blue channels and then dispersed at $R \approx 2000$. The resulting spectra are then mapped onto a regular grid of $0''.5$ square spaxels, with continuous wavelength coverage between 3600 and 10300 Å. For an in-depth discussion of the MaNGA data reduction pipeline, see Law et al. (2016).

The reduced data are analyzed by the MaNGA data analysis pipeline (DAP; Belfiore et al. 2019; Westfall et al. 2019), which extracts stellar kinematics, measures the strengths of continuum features, and extracts emission line fluxes, equivalent widths, and kinematics for each galaxy. For this work, we make use of the emission line fluxes from the DAP’s hybrid binning scheme. In this scheme, the data cubes are Voronoi-binned (Cappellari & Copin 2003) to an S/N of at least 10 in the continuum. Within each of these bins, pPXF (Cappellari & Emsellem 2004) is used to fit an optimal continuum template that is made up of a linear combination of hierarchically clustered templates from the MILES stellar library (Sánchez-Blázquez et al. 2006; Falcón-Barroso et al. 2011), as well as an eighth-degree multiplicative Legendre polynomial. This optimal continuum template constrains the stellar populations within the Voronoi bin and is fitted by pPXF in conjunction with a set of Gaussian emission line templates to each individual spaxel in the bin. For a full description of the DAP fitting process, see Westfall et al. (2019), and for a discussion of the robustness of the emission line measurements, see Belfiore et al. (2019).

2.2. Sample Selection

Galaxies in the MaNGA survey are selected such that the full sample has a roughly flat distribution of stellar masses. However, this parent sample contains galaxies with a wide range of morphologies and star formation rates. Our goal with this work is to make spatially resolved measurements of the properties of the gas in galaxies as a function of the local environment. The metallicity indicators mentioned in Section 2.3 are only calibrated for H II regions and therefore cannot be applied to a fraction of the spaxels in MaNGA. To make this determination, we compare the [N II] $\lambda 6584/H\alpha$ and [O III] $\lambda 5007/H\beta$ emission line ratios on a Baldwin et al. (1981) (BPT) diagram. Only spaxels with emission line ratios that satisfy both the Kewley et al. (2001) and Kauffmann et al. (2003) criteria for excitation of the gas by a young stellar population are included in our analysis. We further exclude spaxels for which the S/Ns in the emission lines used for the metallicity and determination of star formation are less than 3. Belfiore et al. (2019) showed that the fluxes of lines above this

threshold in MaNGA are relatively robust to systematic effects. From these constraints, we calculate the fraction of spaxels for a data cube for which we are able to reliably determine a metallicity. In computing this fraction, we include only spaxels where the g -band flux from the data cube is detected at an S/N of 2 or greater. This condition is imposed so that galaxies that do not fully fill the integral field unit field of view are not unduly excluded. Galaxies for which the fraction of spaxels with a measurable metallicity is larger than 60% are retained for our analysis.

We make a further cut on the galaxies in our sample based on our ability to robustly measure their metallicity gradients. Galaxies with an elliptical minor-to-major axis ratio (b/a) of less than 0.6, as determined by the NASA-Sloan Atlas (NSA; Blanton et al. 2011) elliptical Petrosian photometry, were excluded to give a sample of face-on galaxies. We made a further restriction on the measured r -band effective radius, R_e . Galaxies with $R_e < 4''$ are also rejected. These criteria are motivated by the analysis performed by Belfiore et al. (2017), who showed that beam-smearing effects are nonnegligible for highly inclined systems or galaxies that are small relative to the MaNGA point-spread function. Similarly, Pellegrini et al. (2019) used a set of realistic simulations to show that light-weighted quantities, such as dust attenuation, are systematically overestimated when observed in highly inclined systems.

Our final sample consists of 1008 galaxies with stellar masses in the range $7.8 < \log(M_*/M_\odot) < 11.4$. For the majority of our analysis, we restrict the stellar masses considered to $9 < \log(M_*/M_\odot) < 11$, and in this range, our sample comprises 967 galaxies. The distribution of galaxies in our sample on the color–mass plane is shown in Figure 1.

2.3. Gas-phase Metallicities

To probe the chemical evolution of the galaxies in our sample, we use the DAP emission line measurements to estimate the gas-phase oxygen abundances in these systems. For convenience, we will use the terms “gas-phase oxygen abundance” and “metallicity” interchangeably throughout this work. The estimation of gas-phase oxygen abundances with optical spectroscopy is often achieved by measuring a set of emission line ratios that vary with the conditions of the gas. The metallicity can be calculated by comparing the measured line ratios to theoretical models for H II regions (e.g., Blanc et al. 2015). Alternatively, it can be estimated by using relationships that are empirically calibrated by comparing these line ratios to the spectra of H II regions for which the metallicity has been measured directly using temperature-sensitive emission line ratios, such as [O III] $\lambda 4363/[O III] \lambda 5007$. While it is generally accepted that the direct method of oxygen abundance determination is more robust than theoretical modeling or using empirical calibrations, it is generally not possible with data sets such as MaNGA, as the [O III] $\lambda 4363$ line is typically ~ 100 times fainter than the [O III] $\lambda 5007$ line.

Many of the empirical calibrations suffer from systematics, being biased either high or low due to variations in the ionization parameter in the gas, or contamination from diffuse ionized gas or light from an active galactic nucleus (AGN). To account for this fact, we will make use of two different metallicity calibrations.

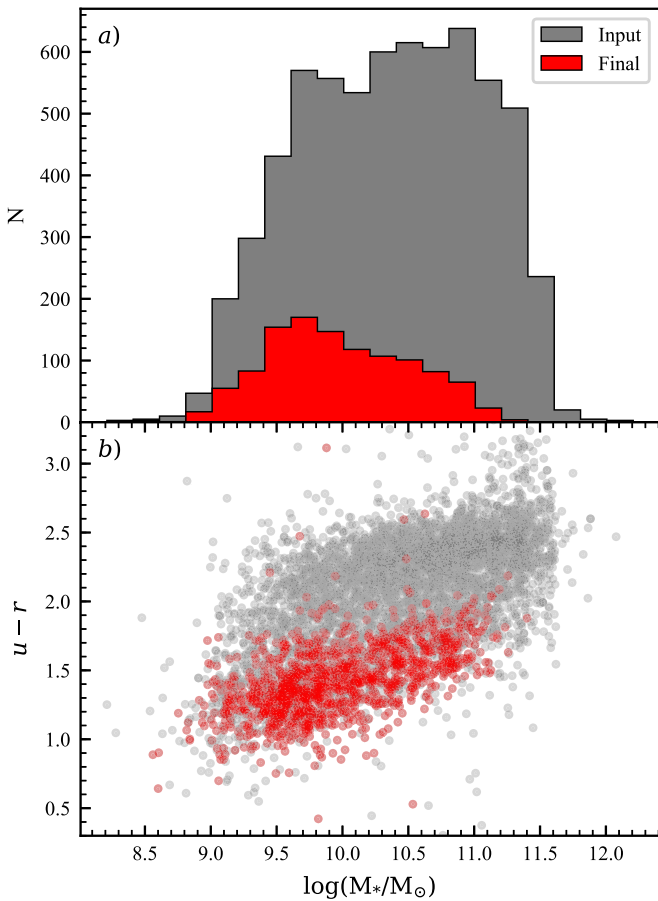


Figure 1. In panel (a), we show the distribution of stellar mass, M_* , for the input (gray) and final (red) samples. The attrition of sources occurs preferentially at high stellar mass, which is consistent with the rising fraction of passive galaxies. In panel (b), the positions of galaxies in the input (gray) and final (red) samples on the $u-r$ color-mass diagram is shown. Galaxies that satisfy our selection criteria are predominantly in the blue cloud and forming stars.

2.3.1. O3N2

For consistency with Barrera-Ballesteros et al. (2018), we use the Pettini & Pagel (2004) O3N2 oxygen abundance diagnostic. This method makes use of the $[\text{O III}] \lambda 5007/\text{H}\beta$ and $[\text{N II}] \lambda 6584/\text{H}\alpha$ emission line ratios and was calibrated against a set of 137 extragalactic H II regions for which a metallicity had been determined either by the direct T_e method or by photoionization modeling of their spectra. Taking $\text{O3N2} = \log([\text{O III}] \lambda 5007/\text{H}\beta) - \log([\text{N II}] \lambda 6584/\text{H}\alpha)$, the metallicity of an H II region can be calculated as

$$12 + \log(\text{O}/\text{H}) = 8.73 - 0.32 \times \text{O3N2} \quad (1)$$

over the range $8.1 < 12 + \log(\text{O}/\text{H}) < 9.05$. It should be noted that this calibration suffers from some degeneracy with variation in the ionization parameter within the gas. For this reason, it cannot be used in spectra that include significant contamination from diffuse ionized gas or AGNs and may also be biased by variations in q between star-forming regions within a galaxy (see, e.g., Poetrodjojo et al. 2018).

2.3.2. N2S2H α

An alternative method for calculating the metallicity of H II regions based on the relative intensities of the $[\text{N II}] \lambda 6584$,

$[\text{S II}] \lambda 6717, 6731$, and $\text{H}\alpha$ lines was presented by Dopita et al. (2016). Assuming a simple relationship between N/O and O/H and modeling theoretical H II regions with a variety of gas pressures and ionization parameters using the MAPPINGS 5.0 software, they found

$$12 + \log(\text{O}/\text{H}) = 8.77 + \log([\text{N II}] \lambda 6584/[\text{S II}] \lambda 6717, 6731) + 0.264 \log([\text{N II}] \lambda 6584/\text{H}\alpha), \quad (2)$$

which they showed has very little dependence on the ionization parameter and is valid over the range $8.0 \lesssim 12 + \log(\text{O}/\text{H}) < 9.05$. There is some evidence that the relationship between N/O and O/H varies with the total stellar mass of a galaxy (Belfiore et al. 2017), but this should be negligible if the analysis is carried out within narrow bins of stellar mass.

Each of the two metallicity calibrations outlined above has different absolute abundance scalings. While it is not possible to directly compare the metallicities of galaxies derived with different calibrations, relative differences between two measurements made with the same indicator are likely to reflect real differences in the chemical composition of the galaxies in question.

2.4. Gas Density

Following the methodology of Barrera-Ballesteros et al. (2018), we estimate the local neutral gas surface density from the dust attenuation derived from the observed Balmer line ratios. Under the assumption of a fixed gas-to-dust ratio, Barrera-Ballesteros et al. (2018) utilized the observation that the gas surface density is related to the V-band attenuation via $\Sigma_{\text{gas}} = 30 \times A_V \text{ pc}^{-2}$. We apply a small correction to this to account for the variation in the dust-to-gas ratio with the gas-phase metallicity using the relation given by Wuyts et al. (2011),

$$\Sigma_{\text{gas}} = 30 \times A_V \times \left(\frac{Z}{Z_\odot}\right)^{-1} \text{ pc}^{-2}, \quad (3)$$

for $Z < Z_\odot$ and independent of metallicity above Z_\odot . In this expression, we calculate the total extinction in the V band as

$$A_V = R_V \times \frac{2.5}{k(\lambda_{\text{H}\beta}) - k(\lambda_{\text{H}\alpha})} \log\left(\frac{f(\text{H}\alpha)/f(\text{H}\beta)}{2.86}\right). \quad (4)$$

For the Cardelli et al. (1989) extinction law, $k(\lambda_{[\text{O III}]}) = 4.77$, $k(\lambda_{[\text{N II}]}) = 2.53$, $k(\lambda_{\text{H}\alpha}) = 2.54$, and $k(\lambda_{\text{H}\beta}) = 3.61$, and the ratio of total to selective extinction, R_V , is 3.1. For our sample (described below), 95% of the spaxels have a metallicity above $0.5 Z_\odot$, meaning that the majority of gas surface density measurements will differ systematically from those derived by Barrera-Ballesteros et al. (2018) by a factor of 2 at most.

2.5. Stellar Mass Surface Density

A large fraction of the baryons in the inner parts of galaxies have been locked away in long-lived stars. The stellar content of a galaxy is therefore a valuable diagnostic for its integrated star formation and chemical enrichment history. For this work, we take the estimates of stellar mass per spaxel provided by Pace et al. (2019a, 2019b). With this method, individual spectra are fitted using a basis set of six vectors, found using principal

component analysis of a permissive set of 40,000 star formation histories. These basis spectra were generated from the C3K library (C. Conroy 2019, in preparation) using a Kroupa (2001) stellar initial mass function. Dust attenuation is taken into account using a two-component model following Charlot & Fall (2000), whereby light from the younger component of the stellar population experiences a different degree of extinction than the light from the older stellar populations. Pace et al. (2019a) showed that this technique provides statistically robust estimates of the stellar mass-to-light ratio across a wide range of S/Ns, star formation histories, and metallicities, with random uncertainties typically 0.1 dex or less for spectra with S/N > 2.

We have rescaled the estimated stellar masses from a Kroupa (2001) to a Chabrier (2003) initial mass function by dividing by 1.06 (Zahid et al. 2012). To calculate the stellar mass surface density (Σ_*) in a spaxel, we take these values and divide them by the projected area of a 0".5 square spaxel at the systemic redshift of the host galaxy. A small correction for the inclination of the galaxy is applied by multiplying these surface densities by the elliptical Petrosian minor-to-major axis ratio.

2.6. Estimating the Local Escape Velocity

We estimate the local escape velocity from the halo assuming a spherically symmetric dark matter halo that is described by a Navarro et al. (1997) Navarro–Frenk–White (NFW) profile using the same procedure as Barrera-Ballesteros et al. (2018). This method assumes that the star-forming gas is confined to a thin disk coplanar with the optical disk and is in a circular orbit around the center of the galaxy. We extract a rotation curve by taking the maximum and minimum measured line-of-sight velocity within a 30° wedge along the photometric major axis of the galaxy, similar to Barrera-Ballesteros et al. (2014). This rotation curve is corrected for the galaxy’s inclination to our line of sight using the r -band elliptical Petrosian major-to-minor axis ratio. We fit the resulting rotation curve using the Böhm et al. (2004) parameterization,

$$V(r_{\text{depro}}) = V_{\text{max}} \frac{r_{\text{depro}}}{(R_{\text{turn}}^\alpha + r_{\text{depro}}^\alpha)^{1/\alpha}}, \quad (5)$$

where V_{max} is the maximum velocity of rotation, r_{depro} is the deprojected radius, R_{turn} is the radius at which the rotation curve flattens, and α is a parameter that determines the shape of the rotation curve. This formulation is a special case of the phenomenological model presented by Courteau (1997). The fitted parameters V_{max} and R_{turn} are then used to derive the local escape velocity using the following formula:

$$V_{\text{esc}}^2 = \begin{cases} V_{\text{esc,in}}^2 + V_{\text{esc,out}}^2 & r_{\text{depro}} < R_{\text{turn}} \\ V_{\text{esc,out}}^2 & r_{\text{depro}} > R_{\text{turn}} \end{cases}, \quad (6)$$

where

$$V_{\text{esc,in}} = (V_{\text{max}}/R_{\text{turn}})^2 (R_{\text{turn}} - r_{\text{depro}})^2 + V_{\text{esc,out}}^2$$

and

$$V_{\text{esc,out}}^2 = 2V_{\text{max}}^2 \ln(R_{\text{vir}}/r_{\text{depro}}) + 2V_{\text{max}}^2.$$

In this relation, R_{vir} is the virial radius of the galaxy’s halo, which we obtain by estimating the galaxy’s total halo mass from its stellar mass using the relation derived by Behroozi et al. (2010).

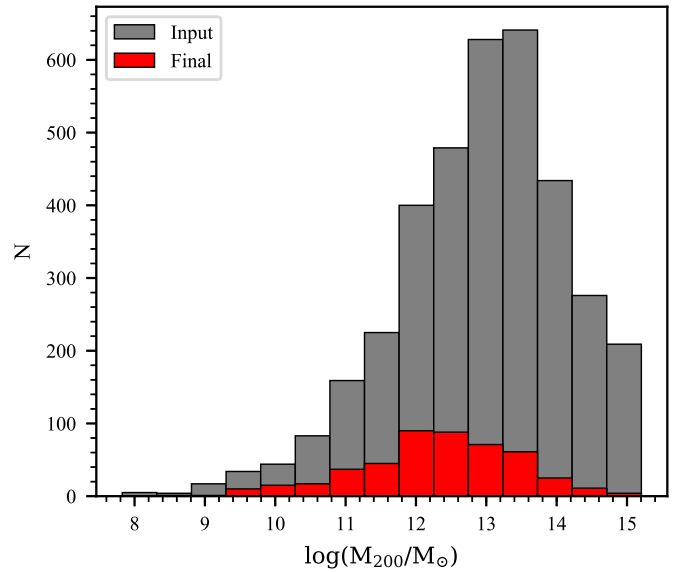


Figure 2. Distribution of group halo mass, M_{200} , for the input (gray) and final (red) samples. The loss of sources from the input sample at higher halo mass is more severe than in low-mass halos due to the higher fraction of passive galaxies in the most dense environments.

This computation of the local escape velocity assumes the galaxy potential to be spherically symmetric. Barrera-Ballesteros et al. (2018) tested how a more complicated two-component halo, which includes a contribution to the gravitational field from the baryons in the galaxy disk, and found that this causes a deviation in the estimated escape velocity of only $\sim 5\%$ from the simpler spherical case.

2.7. Environment

The aim of our current work is to explore how the local environments that galaxies are in today impact their chemical evolution. While there are many different ways of characterizing environment, each capable of tracing a variety of different physical processes that can occur during a galaxy’s lifetime, we will use the satellite/central classification of our sample as the primary metric for environment. This has been shown to be a good predictor of the star-forming properties of galaxies at fixed stellar mass (e.g., Peng et al. 2012). We make use of the Tempel et al. (2017) catalog, which uses a friends-of-friends algorithm to provide estimates of group membership, group richness, and dark matter halo mass for galaxies in the SDSS DR12 (Eisenstein et al. 2011; Alam et al. 2015). Of the 6507 galaxies in MPL-8, 5333 were associated with groups in the Tempel et al. (2017) catalog, of which 3447 are identified as the centrals of their halo and 1886 are satellites. This sample comprises a wide range of group masses, M_{200} , which is the mass contained within R_{200} of the group center, the radius at which the density of an NFW profile drops to 200 times the average density of the universe. Groups within this catalog contain as few as two galaxies and up to 254 members for the most massive halo. We show the distribution of halo masses for our final sample in Figure 2.

2.8. Calculating Metallicity Radial Profiles

To characterize the radial dependence of metallicity in the galaxies in our sample, we construct the radial profile in the

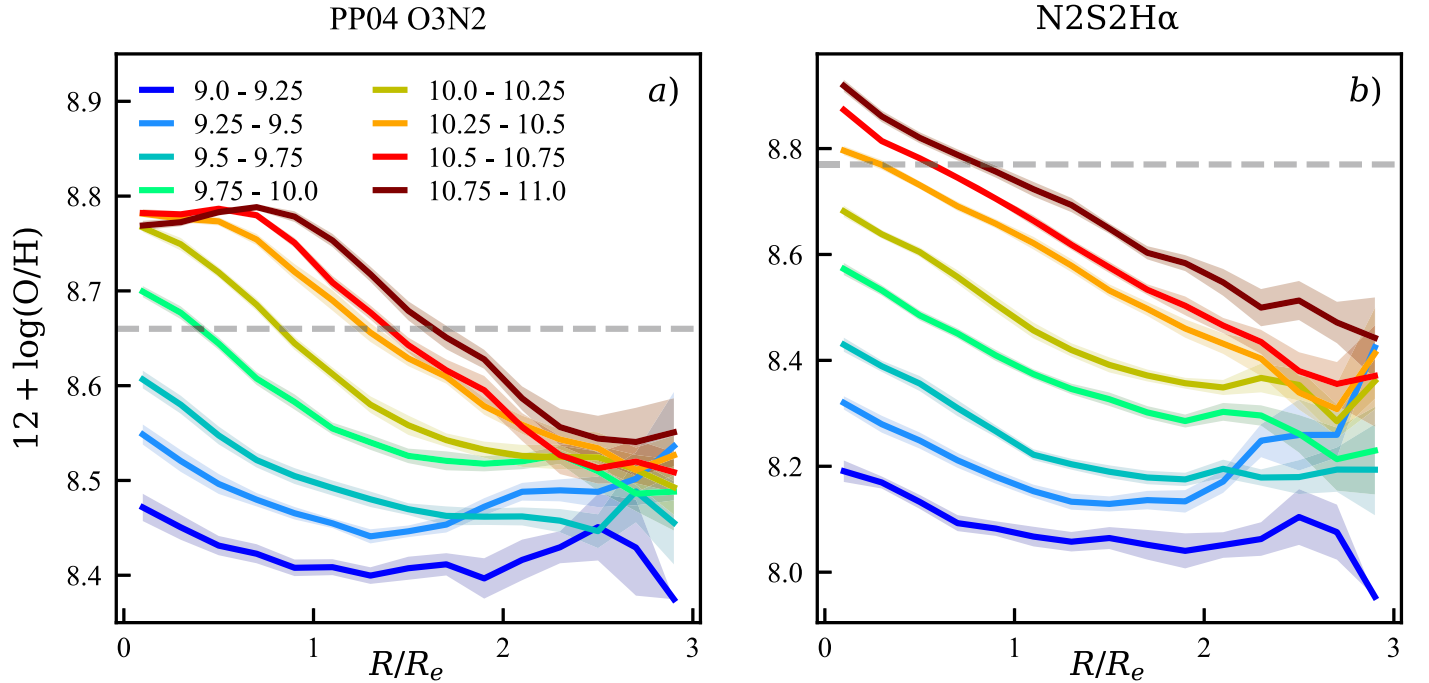


Figure 3. Median metallicity radial profile for galaxies in the stellar mass ranges indicated by the legend at the top of panel (a). The solid curves represent the median profiles, while the shaded regions of the same color represent the 1σ error range on the median. In panel (a), we show the metallicity median profiles made using the Pettini & Pagel (2004) O3N2 indicator, and in panel (b), we show the results from the Dopita et al. (2016) N2S2H α indicator. Note that each metallicity indicator has a different abundance scaling on the y-axis, and in each panel, we mark the assumed solar abundance with a gray dashed line.

following way. In each galaxy, the deprojected distance from the center of the galaxy has been calculated by the DAP based on the r -band surface brightness distribution in the SDSS imaging and assuming each galaxy to be a tilted thin disk. We measure the metallicity as a function of radius and take the average value for spaxels in $0''.5$ wide bins. The metallicity measurements are included only if they are classified as star-forming on the BPT diagram, they have $S/N > 3$ in all emission lines utilized, and the $H\alpha$ equivalent width is greater than 6 \AA in emission. This $H\alpha$ equivalent width criterion is consistent with that chosen by Barrera-Ballesteros et al. (2018) to minimize contamination of the emission line fluxes from diffuse ionized gas.

To understand the behavior of an ensemble of galaxies, we measure what we will call the “median profile” for the metallicity. For this, we take the median of the individual radial profiles within radial bins that are $0.2 R_e$ wide. Once the median has been calculated, we perform a bootstrap resampling of the galaxies, recalculating the median profile for 1000 realizations of the sample. At each radius, the uncertainty on the sample median is estimated to be the standard deviation of the bootstrapped median profiles.

3. Results

3.1. Metallicity Profiles

Following Belfiore et al. (2017), we calculate the median metallicity profiles in narrow bins of stellar mass using two different oxygen abundance indicators. The median profiles for all galaxies in our sample are shown in Figure 3. In panel (a), we show the Pettini & Pagel (2004) O3N2 oxygen abundance median profiles in 0.5 dex wide bins of stellar mass. The profiles shown here are consistent with those shown in Figure 3

of Belfiore et al. (2017), in particular with the steepening of the metallicity gradient at higher stellar mass. Panel (b) shows the profiles for the same galaxies derived using the Dopita et al. (2016) N2S2H α indicator. This indicator shows qualitatively different results than O3N2 in the centers of galaxies above $\log(M/M_\odot) \sim 10.25$. While the N2S2H α metallicities both continue to rise in the centers of massive galaxies, the O3N2 indicator shows a flattening. The origin of the mismatch in the behavior of the metallicity profiles in the centers of massive galaxies between different abundance calibrations may be due to the fact that the Dopita et al. (2016) metallicity calibration is strongly tied to the N/O ratio. Belfiore et al. (2017) showed that N/O increases toward the centers of massive galaxies, while O/H does not.

Again, we caution that the interpretation of metallicity radial profiles from data sets with kiloparsec-scale physical resolution, such as MaNGA, is subject to the flattening of gradients by the observational point-spread function (Yuan et al. 2013; Mast et al. 2014). Carton et al. (2017) presented a method to account for this effect; however, they reported that it was not always robust in the presence of clumpy star formation distributions. Our galaxy size and inclination selection criteria that were outlined in Section 2.2 should mitigate the most severe resolution effects (Belfiore et al. 2017), but we note that the most accurate determinations of metallicity gradients require observations with finer spatial resolution. The core conclusions of this work, particularly those based on local scaling relations, will be only minimally affected by this issue.

3.1.1. Satellites versus Centrals

To investigate the environmental dependence of the radial distribution of the oxygen abundance, we split our sample into

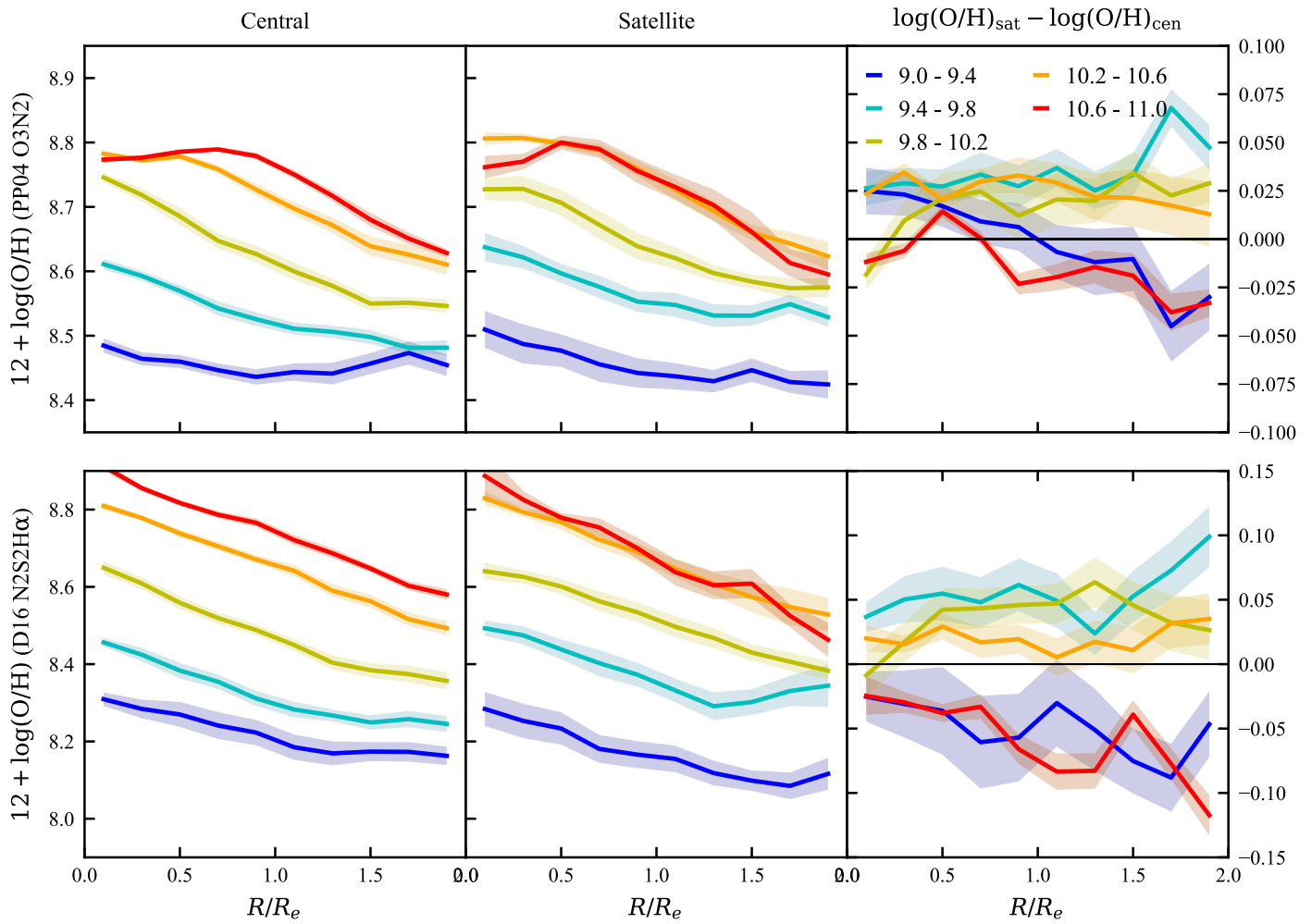


Figure 4. Median metallicity radial profiles in bins of stellar mass split into satellites and centrals. In the upper row, we show the profiles for the O3N2 indicator, while in the lower row, the results for N2S2H α are shown. The profiles for central galaxies are shown in the left column, and those for the satellite galaxies are in the middle column. On the right, we show the difference between the satellites and centrals. Satellite galaxies in the range $9.4 < \log(M_*/M_\odot) < 10.2$ are systematically more metal-rich than centrals of the same mass in both metallicity indicators.

satellites and centrals, then recalculate the median profiles with each metallicity indicator. We show these radial profiles in Figure 4. At fixed stellar mass, there are minor qualitative and quantitative differences between the radial distributions of the oxygen abundance. At all radii, the absolute differences in the median metallicity at fixed stellar mass are less than ~ 0.05 dex for O3N2 and ~ 0.1 dex for N2S2H α . We note that in the highest stellar mass bins, there are very small numbers of star-forming satellites, and their distribution is biased toward the lower stellar masses. For this reason, the differences for the most massive galaxies are not robust in this sample. At lower stellar masses, however, the stellar mass distributions of satellites and centrals are similar, the sample sizes are larger, and a fairer comparison can be made.

Since each metallicity indicator has different systematics and biases, we only deem a difference to be real if it is reflected in both the O3N2 and N2S2H α data. For galaxies in the mass range $9.4 < \log(M_*/M_\odot) < 10.2$, there is a systematic offset in the metallicity, with satellite galaxies being more metal-rich at all radii sampled but with no significant difference in the gradient. In the lowest mass range, the O3N2 indicator shows a

change in the metallicity gradient; however, this is not evident in the N2S2H α metallicity.

3.2. Local Scaling Relations

In addition to the global scaling relations relating a global metallicity measurement to the integrated stellar mass of a galaxy, there are also local correlations between the stellar mass surface density (Moran et al. 2012; Rosales-Ortega et al. 2012) and the local gas-phase metallicity. These local scaling relations capture the response of the chemical abundance of gas to processes occurring on local \sim kiloparsec scales.

3.2.1. Metallicity and Stellar Density

As more stars form and the stellar surface density (Σ_*) increases, the amount of enrichment of the ISM also increases. We explore this relation in Figure 5, where we show the relationship between Σ_* and metallicity for satellite and central galaxies. Hwang et al. (2019) showed that in addition to the relationship between the local Σ_* and $12 + \log(\text{O}/\text{H})$, there is a secondary dependence on the total stellar mass. For this reason,

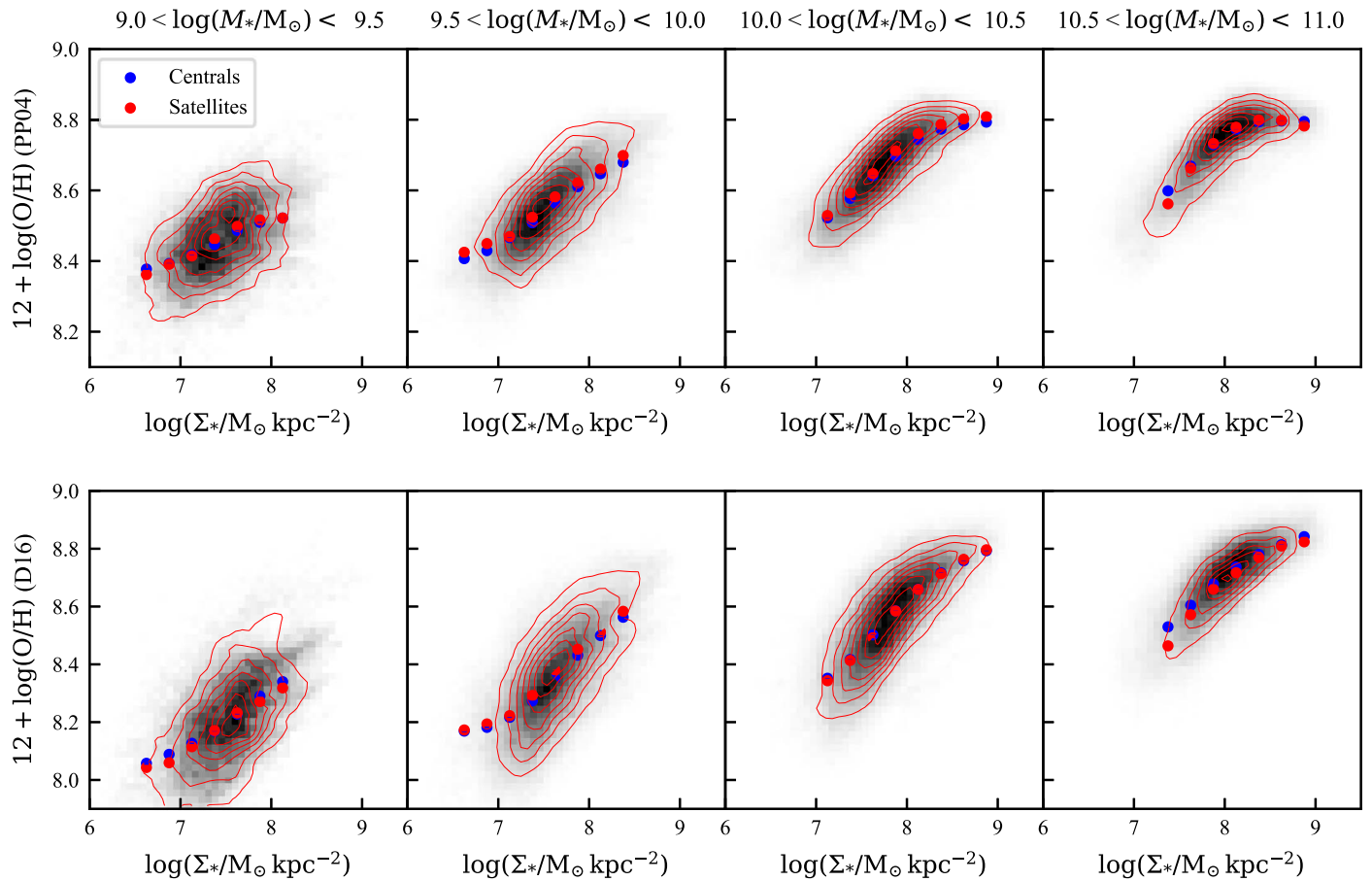


Figure 5. Relationship between local stellar mass surface density and metallicity in bins of total stellar mass for satellite and central galaxies. The gray scale background represents the density of data points for central galaxies, while the red contours represent the distribution of data points from satellite galaxies. For clarity, the distribution for satellite galaxies was smoothed to make the contours less subject to noise. Blue points represent the median values of metallicity in the central galaxies at a fixed Σ_* , and the red points are the medians for satellite galaxies. These are only calculated where there are sufficient data. We include bootstrapped standard errors of the median, but these uncertainties are often smaller than the data points. In the top row, we show the results for the Pettini & Pagel (2004) O3N2 indicator, while in the bottom row, we show the result for the Dopita et al. (2016) N2S2H α indicator. The metallicity of satellite galaxies at a fixed stellar mass surface density is slightly higher (~ 0.01 dex) than for central galaxies.

we have split our analysis into 0.5 dex wide bins of integrated M_* . Using both the O3N2 and N2S2H α , there is a small (~ 0.01 dex) difference between the metallicity at fixed Σ_* between satellites and centrals, particularly in the $9.5 < \log(M_*/M_\odot) < 10$ interval. While the formal uncertainties on the medians indicate that these differences are statistically significant, they are a factor of 10 smaller than the standard deviations of the metallicity distributions. We note that for systems of low stellar mass, a satellite galaxy may occupy a group with a wide range of possible halo masses corresponding to very different environments.

Given that the largest differences in the metallicity between satellites and centrals occurs at the lowest stellar masses, we show the impact of varying the stellar mass of the central in Figure 6. Choosing satellite galaxies in the range $9 < \log(M_*/M_\odot) < 10$, we find a large systematic offset in metallicity for satellites of more massive central galaxies, corresponding to more massive group halos. Satellite galaxies associated with centrals more massive than $\log(M_*/M_\odot) = 10.5$ have metallicities that are, on average, 0.08 ± 0.009 dex higher than those galaxies that are satellites of centrals with $\log(M_*/M_\odot) < 10$. To eliminate the possibility that a different distribution of total stellar masses for

the targeted galaxies within the central stellar mass bin is responsible for the discrepancy, we perform a two-sample Kolmogorov–Smirnov (K-S) test (Smirnov 1939). This test returns a statistic of $D = 0.17$ with $p = 0.71$, indicating no statistically significant difference in the total stellar masses.

3.2.2. Metallicity and Gas Fraction

Models predict (e.g., Lilly et al. 2013) and observations show (Mannucci et al. 2010; Moran et al. 2012) that if low-metallicity gas is accreted onto the galaxy and the local gas fraction rises, then the metal content is diluted and the total metallicity of the gas will decrease. This relationship is investigated in Figure 7, where we show the gas-phase metallicity as a function of the local gas fraction, μ , in intervals of total stellar mass. In narrow bins of stellar mass, we find a tight correlation between the local gas fraction and the metallicity of the ISM. Once again, there is a small difference in the metallicities between satellites and centrals, with the difference being largest in galaxies between $10^{9.5}$ and $10^{10} M_\odot$.

Focusing again on the lower-mass satellite galaxies in our sample, we see in Figure 8 that the satellites of massive

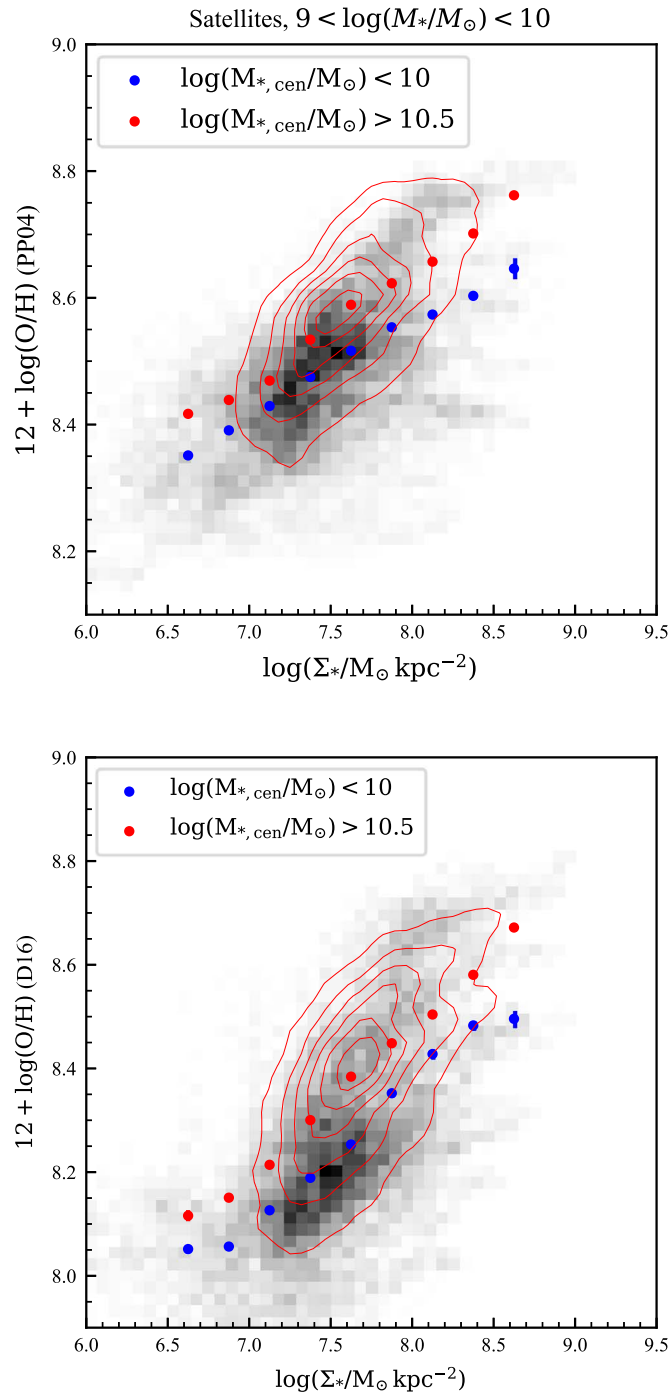


Figure 6. Local Σ_* –O/H relation for satellite galaxies with $9 < \log(M_*/M_\odot) < 10$ split by the mass of the galaxy that is central to their halo. In the upper panel, we show the results for the PP04 indicator, and in the lower panel, we show the results for the D16 indicator. Blue points show the median metallicity at a given Σ_* for satellites of low-mass centrals ($\log(M_*/M_\odot) < 10$). These points trace the median of the gray-shaded distribution. Red points are the median metallicity as a function of Σ_* for satellites of high-mass centrals, shown by the red contours. The oxygen abundance is systematically higher for satellites of more massive centrals.

galaxies are more enriched at fixed μ than the satellites of less massive centrals. Comparing the contours of spaxels in the μ –metallicity plane, we see that, on average, the satellites of more massive centrals have a lower inferred gas fraction. Nevertheless, at fixed μ , the offset in O/H remains.

4. Discussion

4.1. The Impact of Environment on Local Scaling Relations

We have shown that the metallicity versus stellar mass, local escape velocity, and gas fraction local scaling relations vary with the environment that galaxies inhabit. In this study, we utilized the mass of the largest galaxy in the group as our estimate of environment. This quantity is correlated with the total mass of the halo (Behroozi et al. 2010), though it does not suffer from the large uncertainties involved in estimating halo dynamical masses from spectroscopy (see Robotham et al. 2011, for an excellent discussion of this point). For satellite galaxies, the magnitude of the difference in metallicity appears to be a function of the stellar mass of the galaxy that is central to the group. In Figures 6 and 8, we showed that the satellites of central galaxies more massive than $\log M_*/M_\odot > 10.5$ have local metallicities that are enhanced by ~ 0.1 dex over similar galaxies that are satellites of less massive ($\log M_*/M_\odot < 10$) centrals. This enhancement appears to be independent of the local gas fraction and escape velocity.

4.2. Accounting for Outflows with the Gas Regulator Model

While differences in the metallicity of satellite galaxies at fixed Σ_* and μ may be suggestive of some intrinsic difference between the chemical evolution of satellites in different mass halos, these simple scaling relations taken individually are unable to account for all factors that may influence the oxygen abundance. Neither of these scaling relations explicitly accounts for the loss of metals and corresponding reduction in oxygen abundance through outflows. To control for all of these factors at once, we fit the gas regulator model of Lilly et al. (2013) to the data.

The gas regulator model for galaxy evolution makes the simple assumption that a galaxy’s current star formation rate and metallicity are largely determined by the present-day gas fraction. While it was originally devised to apply to galaxies as a whole, some authors have recently shown that it can be applied to galaxies locally on \sim kiloparsec scales (Carton et al. 2015; Barrera-Ballesteros et al. 2018). In their derivation of this model, Lilly et al. (2013) showed that the metal content of galaxies will reach an equilibrium on timescales shorter than the time it takes for their total gas content to be depleted. At equilibrium, the metallicity is

$$Z_{\text{eq}} = Z_0 + \frac{y}{1 + r_{\text{gas}} + (1 - R)^{-1} \left(\lambda + \epsilon^{-1} \frac{d \ln(r_{\text{gas}})}{dt} \right)}, \quad (7)$$

where r_{gas} is the ratio of gas to stellar mass, R is the fraction of gas returned from stars to the ISM by stellar evolution, and ϵ is the star formation efficiency. While this equation contains several unknown quantities, we can fix these to sensible values based on previous estimates from the literature. We adopt a value of $R = 0.4$, which is consistent with the predictions of stellar population synthesis models (Bruzual & Charlot 2003) and in line with the assumptions underlying previous work on this topic (Lilly et al. 2013; Carton et al. 2015; Barrera-Ballesteros et al. 2018). Further, based on fitting the mass–metallicity relation for SDSS galaxies, Lilly et al. (2013) were able to constrain the product $\epsilon^{-1} \frac{d \ln(r_{\text{gas}})}{dt} = -0.25$. The nucleosynthetic yield, y , is also not well known. The yield per stellar generation (and gas return fraction, R) is dependent

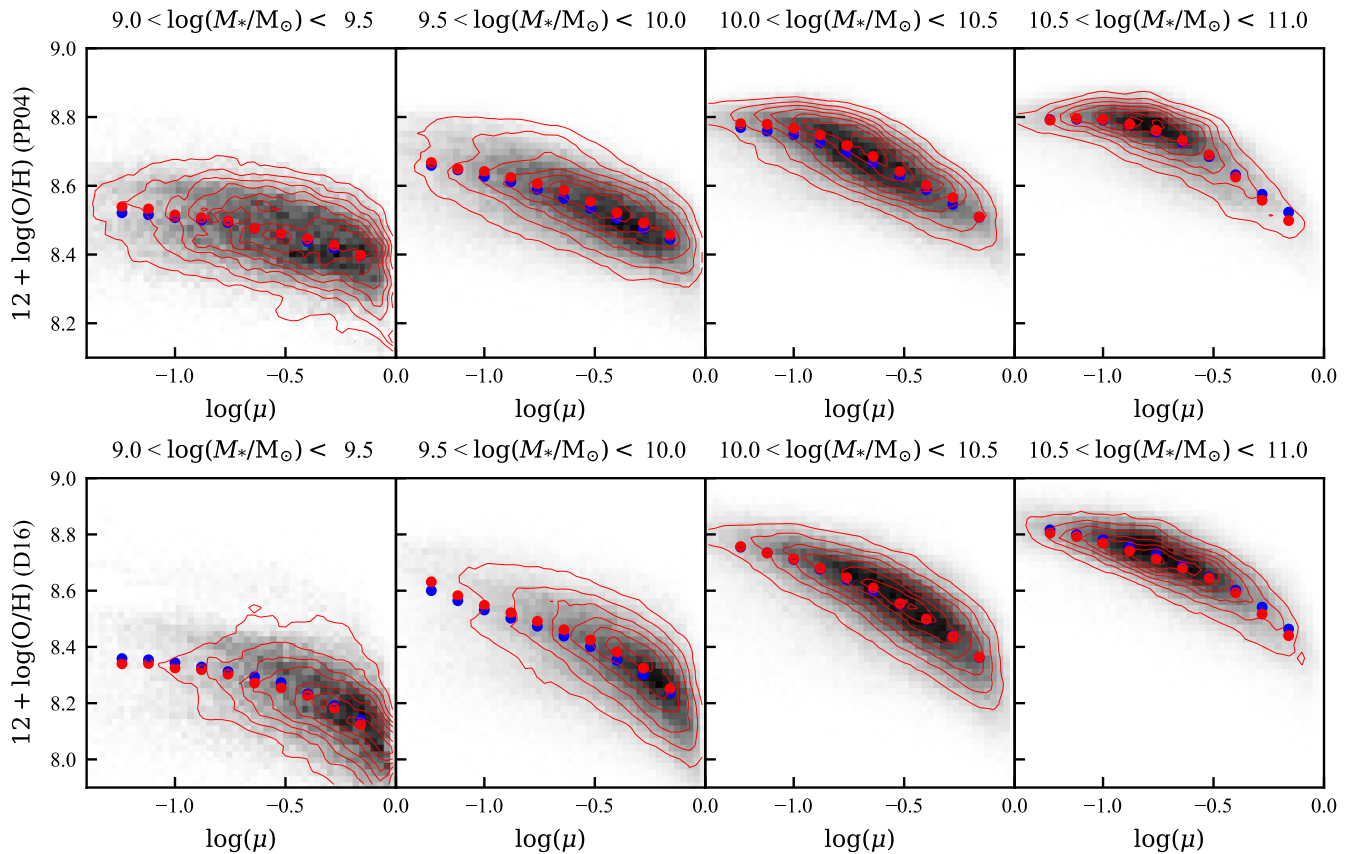


Figure 7. Dependence of $12 + \log(\text{O}/\text{H})$ on the local gas fraction, μ in different bins of stellar mass. The contours, gray scale, and colored points are the same as in Figure 5. The difference in metallicity at fixed μ between satellites and centrals is largest in the range $9.5 < \log(M_*/M_\odot) < 10$, where it reaches ~ 0.015 dex.

on the stellar initial mass function, which some suggest may not be universal (e.g., Gunawardhana et al. 2011; Parikh et al. 2018). Finlator & Davé (2008) estimated the yield to be in the range $0.008 \leq y \leq 0.023$, but we assume a value near the middle of this range of 0.014. This is the value calculated by Barrera-Ballesteros et al. (2018) based on both theoretical modeling using `STARBURST99` (Leitherer et al. 2014) and closed-box modeling of galaxy cluster data (Renzini & Andreon 2014). We assume that this value is constant and valid throughout our entire sample. For a rigorous discussion of the impact of variations of the assumed yield on the calibration and interpretation of metallicities, see Vincenzo et al. (2016).

In the gas regulator model, the outflows are described by the mass-loading factor, λ , which is the ratio of the star formation rate to the rate of mass loss due to stellar feedback and winds. We parameterized the mass-loading factor similar to the formulation of Peebles & Shankar (2011) and assuming the metallicity of outflows is the same as the metallicity in the ISM of the galaxy,

$$\lambda = \left(\frac{v_0}{v_{\text{esc}}(r)} \right)^\alpha. \quad (8)$$

Peebles & Shankar (2011) suggested either $\alpha = 1$ or 2; however, we note that they parameterized λ in terms of the virial velocity of galaxy halos. The relationship between the virial velocity and the local escape velocity is complicated; so, to account for this, we allow α to vary freely. Barrera-Ballesteros et al. (2018) also included an additive constant in

their parameterization of λ , which imposes a minimum level of outflows from even the deepest potential well. For a reasonable choice of yield, we find that this has the effect of limiting the maximum metallicity that a gas-regulated system can achieve.

4.2.1. Fitting the Pettini & Pagel (2004) Metallicity

In order to constrain the values of v_0 and α for our model, we fit Equation (7) to the metallicity, gas fraction, and local escape velocities inferred from the MaNGA spaxel data for all galaxies in our sample. We find $v_0 = 368 \text{ km s}^{-1}$ and $\alpha = 0.52$. In their work on deriving the v_{esc} dependence of λ , Barrera-Ballesteros et al. (2018) noted that the gas regulator model does not necessarily provide a good fit to the data, though it was preferred to the leaky-box model of Zhu et al. (2017) on the grounds that it provided more realistic estimates of λ . In our fits of the gas regulator model to the MaNGA data on kiloparsec scales, we find smaller residuals at a low gas fraction. This is a direct result of our choice not to include an additive constant in our parameterization of λ . In the analysis that follows, we fix the dependence of λ on the escape velocity, reducing this problem to fitting only one variable, the metallicity of accreted gas, Z_0 .

We perform a least-squares fit of the gas regulator model to the O3N2-based gas-phase metallicities, fitting for Z_0 in the subpopulations where the largest difference in metallicity is seen. This is for satellite galaxies with stellar masses in the range $9 < \log(M_*/M_\odot) < 10$, split based on the stellar mass of the corresponding central galaxy. For satellites of low-mass centrals ($\log(M_*/M_\odot) < 10$), the metallicity of the gas precipitating onto

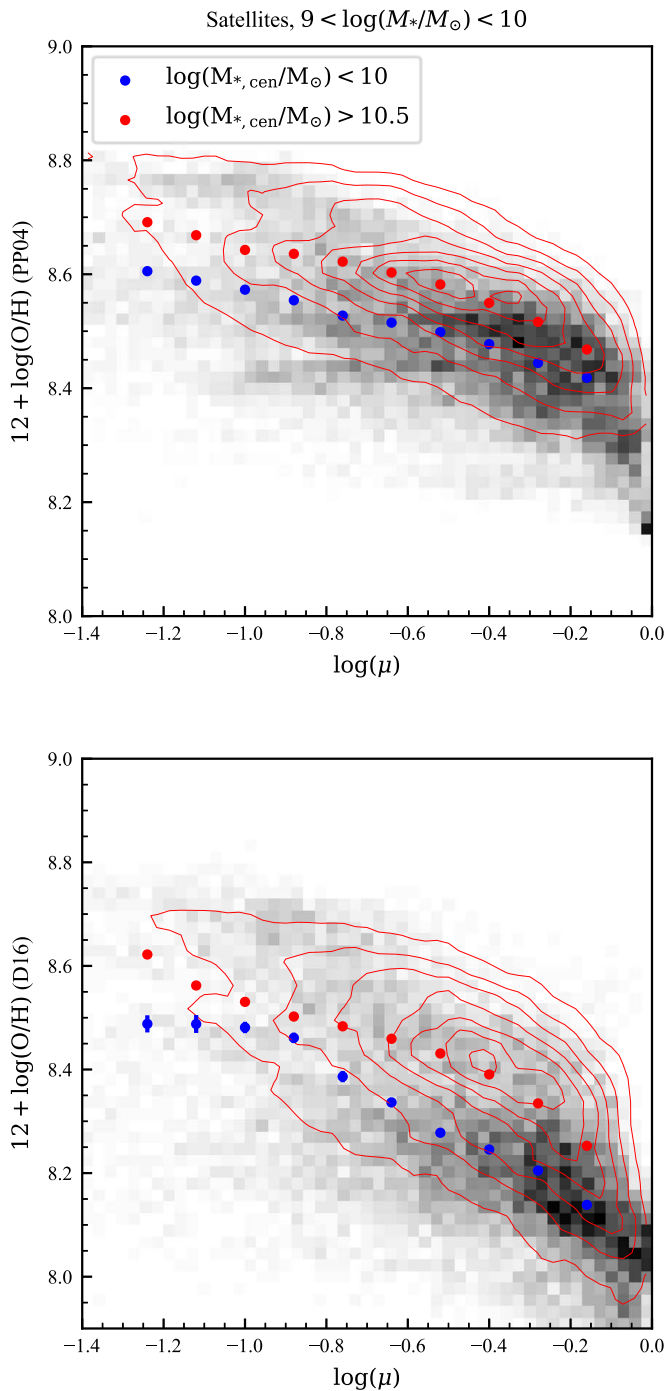


Figure 8. Relationship between μ and O/H for satellites of low-mass (gray background with blue points indicating the medians) and high-mass (red contours with red points indicating the medians) centrals for PP04 O3N2 (top) and D16 N2S2H α (bottom). At a fixed gas fraction, the median metallicity is ~ 0.1 dex higher for the satellites of massive centrals.

their disks inferred from the modeling is $Z_0 = (4.68 \pm 0.11) \times 10^{-4}$, corresponding to $12 + \log(\text{O}/\text{H}) = 7.46 \pm 0.01$. For the gas being accreted onto the $9 < \log(M_*/M_\odot) < 10$ satellites of high-mass central galaxies, we derive a metallicity of $Z_0 = (1.17 \pm 0.001) \times 10^{-3}$, or $12 + \log(\text{O}/\text{H}) = 7.87 \pm 0.003$.

4.2.2. Fitting the Dopita et al. (2016) Metallicity

The metallicities derived from the Dopita et al. (2016) N2S2H α calibration have a different absolute abundance

scaling and cover a larger range for the same set of spectra. This can be seen by comparing the y-axes in Figure 5. Using the same values of the yield and gas return fraction as were used to fit the O3N2 metallicities, the data favor a negative value of Z_0 , which is unphysical. With this indicator, the values of λ allowed by this parameterization that also gives an appropriate shape to the distribution of modeled data in the μ - Z plane are too large. Using the λ parameterization of Barrera-Ballesteros et al. (2018), $\lambda = (v_0/v_{\text{esc}})^\alpha + \lambda_0$, we find $Z_0 = (3.0 \pm 0.12) \times 10^{-4}$ or $12 + \log(\text{O}/\text{H}) = 7.27 \pm 0.01$ for the satellites of low-mass centrals. For the satellites of high-mass centrals, we find $Z_0 = (8.6 \pm 0.1) \times 10^{-4}$ or $12 + \log(\text{O}/\text{H}) = 7.86 \pm 0.003$.

We note that the absolute value for these inferred quantities is correlated with a number of unconstrained parameters, including the nucleosynthetic yield of oxygen, y ; the gas return fraction from stars, R ; and the precise form of the mass-loading factor, λ . Nevertheless, we argue that the assumption that these parameters do not vary between star-forming galaxies in a relatively narrow mass range is reasonable, and that the choice to fix them for this comparison is justified. With this limitation, it is not possible to derive an absolute abundance for the accreted gas, but the existence of a difference is robust. As was shown in Figures 6 and 8, the difference in local metallicity scaling relations is significant between these two galaxy subpopulations. The gas regulator model provides an interpretive framework to describe these differences in terms of the variation of the metallicity of the intergalactic medium in different environments while controlling for small differences in the estimated local gas fraction and escape velocity.

4.3. Can Starvation Explain Our Results?

Our results are analogous to those seen by previous studies of the environmental dependence of the global mass-metallicity relation (e.g., Cooper et al. 2008; Pasquali et al. 2012; Peng & Maiolino 2014; Wu et al. 2017). While different studies have found qualitatively similar results, there is considerable disagreement in the interpretation. Peng & Maiolino (2014) argued that the primary driver of this trend must be the elevation of the metallicity of gas being accreted onto galaxies in dense environments. This argument hinges on their observation that the distribution of star formation rates in their sample is independent of environment. This conclusion contrasts starkly with the interpretation of Wu et al. (2017), who suggested that the environmental variation of the mass-metallicity relation can be explained by the reduction in the gas fractions of galaxies with the local galaxy overdensity.

Starvation, whereby the accretion of gas onto galaxies is curtailed and the gas reservoir is not replenished following star formation (Larson et al. 1980), will have the effect of increasing the gas-phase metallicity of a galaxy or a region of the galaxy. This is a natural consequence of maintaining a constant metal yield from stellar evolution while reducing the replenishment of the reservoir with relatively low-metallicity gas. Within the framework of gas-regulated galaxy evolution, this implies an anticorrelation between the gas surface density or star formation rate surface density and the metallicity in the gas. Starvation has been suggested as a key component for determining the star-forming properties of galaxies today (Peng et al. 2015; Trussler et al. 2018), with environment appearing to play a role in instigating this process (von der Linden et al. 2010; Davies et al. 2016).

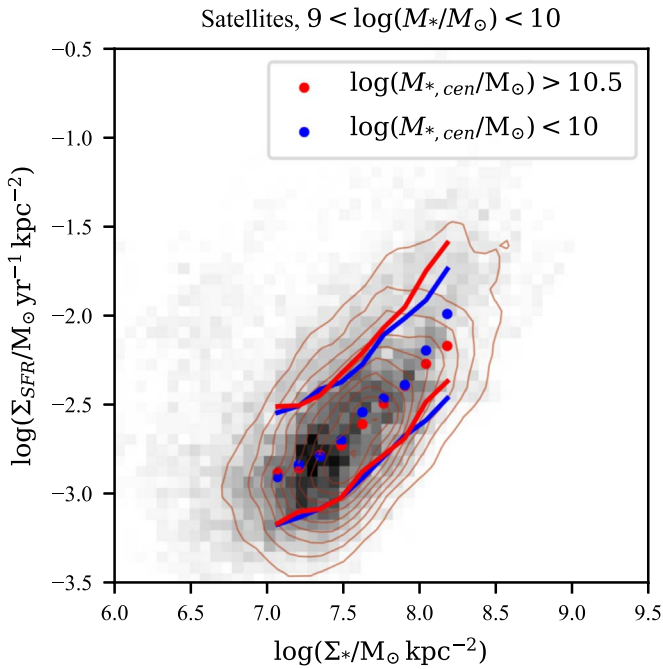


Figure 9. Star formation rate surface density as a function of stellar mass surface density for galaxies with $9 < \log(M_*/M_\odot) < 10$. The gray scale shows the distribution of measurements from satellites of low-mass centrals ($\log(M_{*,cen}/M_\odot) < 10$), with the median of this distribution shown by blue points and the 16th and 84th percentiles shown by blue lines. The red contours indicate the Σ_* - Σ_{SFR} distribution for satellites of massive galaxies ($\log(M_{*,cen}/M_\odot) > 10.5$), with the red points showing the median and the red lines marking the 16th and 84th percentiles of the distribution. There is very little difference in the two distributions for the vast majority of spaxels in the two samples.

While we do infer gas fractions that are, on average, lower for galaxies that are in more extreme environments (for example, low-mass satellites of high-mass galaxies), we find that at a fixed gas fraction, the metallicity is higher for satellites relative to centrals, even in spaxels with high μ . The differing distributions of $\log(\mu)$ evident in Figure 8 are largely driven by the differences in the distributions of Σ_* . Although the distributions of total M_* between the two subsamples used are not significantly different, the distributions of local stellar mass surface densities are. In Figure 9, we show the joint distributions for Σ_* and Σ_{SFR} for low-mass satellites, split by the stellar mass of the central galaxy. At fixed Σ_* , the difference between the means of the Σ_{SFR} is smaller than 0.03 dex, except above $\log(\Sigma_*) = 8.1$, but this range accounts for only $\sim 10\%$ of the data and therefore has a minimal impact on our model fitting.

It is possible that the distribution of star formation has also changed. Schaefer et al. (2019) showed that in dense environments, the outer parts of a galaxy can be quenched, leaving star formation in the inner regions unaffected. This transformation was nevertheless accompanied by a reduction in the total specific star formation rate (sSFR). To test for this, we perform a K-S test on the integrated sSFRs of the two subsamples. This yields $K-S = 0.17$ with $p = 0.58$. Furthermore, the median of the sSFR for the satellites of high-mass galaxies is $-10.12 \pm 0.07 \text{ yr}^{-1}$, and the median for the satellites of more massive galaxies is $-10.21 \pm 0.04 \text{ Gyr}^{-1}$, where the error on the median has been estimated using a bootstrap resampling. The difference of the medians is within the error margin.

The similar distributions of Σ_{SFR} and sSFR disfavor the interpretation that the changing gas fraction due to starvation is responsible for the environmental differences in metallicity on kiloparsec scales within our sample. This is not to say that starvation does not occur in dense environments; our sample selection simply favors the most star-forming galaxies, which are unlikely to have had their star formation rates reduced by environmental effects yet. Environmental differences in metallicity may occur in satellite galaxies before the onset of environment quenching.

4.4. Comparison to Simulations

Numerical simulations of galaxy evolution are beginning to show that the gas being accreted onto galaxies cannot be assumed to be pristine in all environments (Oppenheimer et al. 2010; Gupta et al. 2018). In the simulations, the origin of accreted gas is observed to be highly dependent on redshift, with cosmological accretion of low-metallicity gas dominating at high redshift. However, as time progresses, feedback from star formation and AGN activity expels gas from the ISMs of galaxies, which enriches their local environment with material that subsequently falls onto their neighbors. In the FIRE simulations, Anglés-Alcázar et al. (2017) found that the exchange of gas between galaxies that is facilitated by galactic winds dominates the accretion budget by $z = 0$.

Gupta et al. (2018) explored this effect using data from the IllustrisTNG simulations. They showed that the enrichment of the intergalactic medium and the associated accretion onto galaxies is dependent on both the halo mass and whether a galaxy is infalling into its host halo or has been a satellite for some time. At $z < 0.5$, they found that the metallicity of gas being accreted onto galaxies with $9 < \log(M_*/M_\odot) < 10$ that are infalling into clusters is approximately $0.35 Z_\odot$, which is 1.5–2 times more metal-rich than for similar galaxies in the field. This is consistent with the metallicity difference that we have inferred between the satellites of low- and high-mass centrals, though the absolute abundances differ. We again note that the value of Z_0 returned when the model represented by Equation (7) is fitted to the data is sensitive to the precise values of the yield, y , and the gas return fraction, R , which are not well constrained by observations. The choice of these values will change the estimate of Z_0 , but the relative difference between subsamples will not be greatly affected.

4.5. Other Studies of the Environmental Dependence of Metallicity

The impact of environment on galaxy evolution, in particular star formation and metallicity, is subtle. For this reason, there have been very few observational works that measure the impact of environment on the spatial patterns of chemical abundances in galaxies. It has only been recently that large enough samples of integral field spectroscopic data have become available to adequately measure these effects.

In a recent study, Lian et al. (2019) used MaNGA data to study the metallicity gradients of galaxies as a function of the local environmental overdensity. They found that the metallicity gradients in low-mass satellite galaxies are shallower in dense environments, with a higher metallicity in their outer parts than similar galaxies in the field. They also found that the star formation rate gradients in galaxies in dense environments are steeper and concluded that the most likely explanation for

these observations is a variation in the gas accretion timescale in different environments. Superficially, this would seem to contradict our results, but we argue that this apparent disagreement can be resolved by noting the differences between the samples of galaxies considered. Lian et al. placed less stringent constraints on the number of star-forming spaxels than we do, meaning that their galaxies have lower sSFRs, on average. They therefore studied galaxies that are likely to have inhabited their host halos for a longer period of time and are more affected by environment quenching processes. This point is made in Section 4.3, where we rule out starvation as the primary driver of the environmental effects discussed in this work. Additionally, we note that Lian et al. (2019) placed no constraints on the inclination of galaxies in their sample to the line of sight. This may explain the differences in the metallicity gradients from those reported in our work.

5. Conclusions

We have estimated local metallicities, gas fractions, escape velocities, and star formation rate surface densities for a sample of nearly face-on star-forming galaxies observed by MaNGA. In this sample, we have explored the impact of the environment on local scaling relations between these estimated quantities, with a particular focus on satellite galaxies. We find the following.

1. At fixed stellar mass, we find a small but global offset of 0.025 (for O3N2) or 0.05 (for N2S2H α) dex in the metallicities of galaxies between satellites and centrals. For our sample, we find little evidence for changes in the metallicity gradient between satellites and centrals.
2. The disparity between the metallicity of satellites and centrals is also evident in the O/H— Σ_* and O/H— μ local scaling relations. We find the greatest offset when we split our satellite sample by the stellar mass of the galaxy that is central to the respective halo. For satellite galaxies in the range $9 < \log(M_*/M_\odot) < 10$, the local scaling relations are ~ 0.1 dex more oxygen-rich for satellites of hosts more massive than $10^{10.5} M_\odot$ than for hosts less massive than $10^{10} M_\odot$.
3. The offset in metallicity for satellite galaxies is found to exist between different environments at a constant stellar mass surface density, gas mass fraction, and star formation rate surface density. From these, we conclude that the observed differences cannot be explained by gas starvation occurring in satellites around more massive centrals. Interestingly, the impact of environment on the chemical enrichment of galaxies appears to precede the onset of the quenching of star formation in their disks.
4. Measured on kiloparsec scales, local metallicities and gas fractions are found to be quantitatively consistent with the gas regulator model of Lilly et al. (2013). We assume that the mass-loading factor describing outflows in galaxies is a function of the local escape velocity. Within the framework of the gas regulator model, the only explanation for the elevated metallicity is an increase in Z_0 for satellites of high-mass galaxies. We estimate that the oxygen abundance in the inflowing gas changes from $12 + \log(\text{O}/\text{H}) = 7.54 \pm 0.01$ to 7.86 ± 0.003 using the Pettini & Pagel (2004) O3N2 indicator, or $12 + \log(\text{O}/\text{H}) = 7.27 \pm 0.01$ to 7.86 ± 0.003 for N2S2H α .

Given these conclusions, we interpret the enhanced metallicity of the satellites of more massive centrals to be evidence for the exchange of enriched gas between galaxies. In this picture, which has been motivated by both observations (Peng & Maiolino 2014) and simulations (Oppenheimer et al. 2010; Anglés-Alcázar et al. 2017; Gupta et al. 2018), feedback-driven winds expel metal-rich gas from a massive star-forming central that is subsequently accreted onto nearby satellites. While our estimates for the metallicity of gas accreted onto satellite galaxies are a factor of ~ 3 lower than the predictions of Gupta et al. (2018), we note that the values returned by our modeling are subject to inherent uncertainties in the nucleosynthetic yield, the gas return fraction from stellar evolution, and the absolute abundance scaling of the strong-line metallicity diagnostics. Notwithstanding these systematic effects, the inferred differential in the metallicity of gas accreted onto satellites in different environments is qualitatively in good agreement with the simulations.




The impact of environment on the gas-phase metallicity distribution of galaxies is likely to be complicated and multifaceted. In addition to the accretion of enriched gas in dense environments that we have studied here, tidal interactions, mergers, and ram pressure can influence the distribution of metals in a galaxy. A complete understanding of the effect of environment on gas-phase metallicities must take these other processes into account. A more comprehensive analysis of the detailed environmental dependence of the chemical properties of galaxies will be made possible when the full MaNGA sample becomes available or with future integral field spectroscopic surveys such as HECTOR (Bryant et al. 2016).

A.L.S., Z.J.P., and C.T. acknowledge NSF CAREER award AST-1554877. A.J. acknowledges NSF award 1616547. R.M. acknowledges ERC Advanced grant 695671 “QUENCH” and support from the the Science and Technology Facilities Council (STFC).

This research made use of *Astropy*, a community-developed core python package for astronomy (Astropy Collaboration et al. 2013, 2018); *matplotlib* (Hunter 2007), an open-source python plotting library; and *LMFIT* (Newville et al. 2014), an interface for nonlinear optimization in python. Funding for the Sloan Digital Sky Survey IV has been provided by the Alfred P. Sloan Foundation, the U.S. Department of Energy Office of Science, and the Participating Institutions. The SDSS acknowledges support and resources from the Center for High-Performance Computing at the University of Utah. The SDSS website is www.sdss.org. The SDSS is managed by the Astrophysical Research Consortium for the Participating Institutions of the SDSS Collaboration, including the Brazilian Participation Group, the Carnegie Institution for Science, Carnegie Mellon University, the Chilean Participation Group, the French Participation Group, Harvard-Smithsonian Center for Astrophysics, Instituto de Astrofísica de Canarias, The Johns Hopkins University, Kavli Institute for the Physics and Mathematics of the Universe (IPMU)/University of Tokyo, the Korean Participation Group, Lawrence Berkeley National Laboratory, Leibniz Institut für Astrophysik Potsdam (AIP), Max-Planck-Institut für Astronomie (MPIA Heidelberg), Max-Planck-Institut für Astrophysik (MPA Garching), Max-Planck-Institut für Extraterrestrische Physik (MPE), National Astronomical Observatories of China, New Mexico State University, New York University, the

University of Notre Dame, Observatório Nacional/MCTI, The Ohio State University, Pennsylvania State University, Shanghai Astronomical Observatory, the United Kingdom Participation Group, Universidad Nacional Autónoma de México, the University of Arizona, the University of Colorado Boulder, the University of Oxford, the University of Portsmouth, the University of Utah, the University of Virginia, the University of Washington, the University of Wisconsin, Vanderbilt University, and Yale University.

ORCID iDs

Zachary Pace  <https://orcid.org/0000-0003-4843-4185>
 Francesco Belfiore  <https://orcid.org/0000-0002-2545-5752>
 Matthew A. Bershadly  <https://orcid.org/0000-0002-3131-4374>
 Niv Drory  <https://orcid.org/0000-0002-7339-3170>
 David Stark  <https://orcid.org/0000-0002-3746-2853>
 David Wake  <https://orcid.org/0000-0002-6047-1010>
 Renbin Yan  <https://orcid.org/0000-0003-1025-1711>

References

- Aguado, D. S., Ahumada, R., Almeida, A., et al. 2019, *ApJS*, **240**, 23
- Alam, S., Albareti, F. D., Allende Prieto, C., et al. 2015, *ApJS*, **219**, 12
- Anglés-Alcázar, D., Faucher-Giguère, C.-A., Kereš, D., et al. 2017, *MNRAS*, **470**, 4698
- Astropy Collaboration, Price-Whelan, A. M., Sipőcz, B. M., et al. 2018, *AJ*, **156**, 123
- Astropy Collaboration, Robitaille, T. P., Tollerud, E. J., et al. 2013, *A&A*, **558**, A33
- Baldwin, J. A., Phillips, M. M., & Terlevich, R. 1981, *PASP*, **93**, 5
- Barrera-Ballesteros, J. K., Falcón-Barroso, J., García-Lorenzo, B., et al. 2014, *A&A*, **568**, A70
- Barrera-Ballesteros, J. K., Heckman, T., Sánchez, S. F., et al. 2018, *ApJ*, **852**, 74
- Barrera-Ballesteros, J. K., Heckman, T. M., Zhu, G. B., et al. 2016, *MNRAS*, **463**, 2513
- Behroozi, P. S., Conroy, C., & Wechsler, R. H. 2010, *ApJ*, **717**, 379
- Belfiore, F., Maiolino, R., Tremonti, C., et al. 2017, *MNRAS*, **469**, 151
- Belfiore, F., Westfall, K. B., Schaefer, A., et al. 2019, *AJ*, **158**, 160
- Birnboim, Y., & Dekel, A. 2003, *MNRAS*, **345**, 349
- Blanc, G. A., Kewley, L., Vogt, F. P. A., & Dopita, M. A. 2015, *ApJ*, **798**, 99
- Blanton, M. R., Kazin, E., Muna, D., Weaver, B. A., & Price-Whelan, A. 2011, *AJ*, **142**, 31
- Böhm, A., Ziegler, B. L., Saglia, R. P., et al. 2004, *A&A*, **420**, 97
- Bothwell, M. S., Maiolino, R., Kennicutt, R., et al. 2013, *MNRAS*, **433**, 1425
- Brook, C. B., Stinson, G., Gibson, B. K., et al. 2014, *MNRAS*, **443**, 3809
- Bruzual, G., & Charlot, S. 2003, *MNRAS*, **344**, 1000
- Bryant, J. J., Bland-Hawthorn, J., Lawrence, J., et al. 2016, *Proc. SPIE*, **9908**, 99081F
- Bryant, J. J., Owers, M. S., Robotham, A. S. G., et al. 2015, *MNRAS*, **447**, 2857
- Bundy, K., Bershadly, M. A., Law, D. R., et al. 2015, *ApJ*, **798**, 7
- Cano-Díaz, M., Sánchez, S. F., Zibetti, S., et al. 2016, *ApJL*, **821**, L26
- Cappellari, M., & Copin, Y. 2003, *MNRAS*, **342**, 345
- Cappellari, M., & Emsellem, E. 2004, *PASP*, **116**, 138
- Cardelli, J. A., Clayton, G. C., & Mathis, J. S. 1989, *ApJ*, **345**, 245
- Carton, D., Brinchmann, J., Shirazi, M., et al. 2017, *MNRAS*, **468**, 2140
- Carton, D., Brinchmann, J., Wang, J., et al. 2015, *MNRAS*, **451**, 210
- Chabrier, G. 2003, *PASP*, **115**, 763
- Charlot, S., & Fall, S. M. 2000, *ApJ*, **539**, 718
- Chisholm, J., Tremonti, C., & Leitherer, C. 2018, *MNRAS*, **481**, 1690
- Cooper, M. C., Tremonti, C. A., Newman, J. A., & Zabludoff, A. I. 2008, *MNRAS*, **390**, 245
- Courteau, S. 1997, *AJ*, **114**, 2402
- Croom, S. M., Lawrence, J. S., Bland-Hawthorn, J., et al. 2012, *MNRAS*, **421**, 872
- Davies, L. J. M., Robotham, A. S. G., Driver, S. P., et al. 2016, *MNRAS*, **455**, 4013
- D'Eugenio, F., Colless, M., Groves, B., Bian, F., & Barone, T. M. 2018, *MNRAS*, **479**, 1807
- Dopita, M. A., Kewley, L. J., Sutherland, R. S., & Nicholls, D. C. 2016, *Ap&SS*, **361**, 61
- Eisenstein, D. J., Weinberg, D. H., Agol, E., et al. 2011, *AJ*, **142**, 72
- Erb, D. K. 2008, *ApJ*, **674**, 151
- Falcón-Barroso, J., Sánchez-Blázquez, P., Vazdekis, A., et al. 2011, *A&A*, **532**, A95
- Fielding, D., Quataert, E., McCourt, M., & Thompson, T. A. 2017, *MNRAS*, **466**, 3810
- Finlator, K., & Davé, R. 2008, *MNRAS*, **385**, 2181
- Gunawardhana, M. L. P., Hopkins, A. M., Sharp, R. G., et al. 2011, *MNRAS*, **415**, 1647
- Gunn, J. E., & Gott, J. R., III 1972, *ApJ*, **176**, 1
- Gunn, J. E., Siegmund, W. A., Mannery, E. J., et al. 2006, *AJ*, **131**, 2332
- Gupta, A., Yuan, T., Torrey, P., et al. 2018, *MNRAS*, **477**, L35
- Heckman, T. M., Armus, L., & Miley, G. K. 1990, *ApJS*, **74**, 833
- Hunter, J. D. 2007, *CSE*, **9**, 90
- Hwang, H.-C., Barrera-Ballesteros, J. K., Heckman, T. M., et al. 2019, *ApJ*, **872**, 144
- Kacprzak, G. G., van de Voort, F., Glazebrook, K., et al. 2016, *ApJL*, **826**, L11
- Kauffmann, G., Heckman, T. M., Tremonti, C., et al. 2003, *MNRAS*, **346**, 1055
- Kewley, L. J., Dopita, M. A., Sutherland, R. S., Heisler, C. A., & Trevena, J. 2001, *ApJ*, **556**, 121
- Kroupa, P. 2001, *MNRAS*, **322**, 231
- Larson, R. B. 1972, *NPhS*, **236**, 7
- Larson, R. B., Tinsley, B. M., & Caldwell, C. N. 1980, *ApJ*, **237**, 692
- Law, D. R., Cherinka, B., Yan, R., et al. 2016, *AJ*, **152**, 83
- Law, D. R., Yan, R., Bershadly, M. A., et al. 2015, *AJ*, **150**, 19
- Lehner, N., Howk, J. C., Tripp, T. M., et al. 2013, *ApJ*, **770**, 138
- Leitherer, C., Ekström, S., Meynet, G., et al. 2014, *ApJS*, **212**, 14
- Lian, J., Thomas, D., Li, C., et al. 2019, *MNRAS*, **489**, 1436
- Lilly, S. J., Carollo, C. M., Pipino, A., Renzini, A., & Peng, Y. 2013, *ApJ*, **772**, 119
- Maiolino, R., & Mannucci, F. 2019, *A&ARv*, **27**, 3
- Mannucci, F., Cresci, G., Maiolino, R., Marconi, A., & Gnerucci, A. 2010, *MNRAS*, **408**, 2115
- Mast, D., Rosales-Ortega, F. F., Sánchez, S. F., et al. 2014, *A&A*, **561**, A129
- Medling, A. M., Cortese, L., Croom, S. M., et al. 2018, *MNRAS*, **475**, 5194
- Moran, S. M., Heckman, T. M., Kauffmann, G., et al. 2012, *ApJ*, **745**, 66
- Navarro, J. F., Frenk, C. S., & White, S. D. M. 1997, *ApJ*, **490**, 493
- Newville, M., Stensitzki, T., Allen, D. B., & Ingargiola, A. 2014, LMFIT: Non-Linear Least-Square Minimization and Curve-Fitting for Python v0.9.13, Zenodo, doi:10.5281/zenodo.11813
- Oppenheimer, B. D., Davé, R., Kereš, D., et al. 2010, *MNRAS*, **406**, 2325
- Pace, Z. J., Tremonti, C., Chen, Y., et al. 2019a, *ApJ*, **883**, 82
- Pace, Z. J., Tremonti, C., Chen, Y., et al. 2019b, *ApJ*, **883**, 83
- Parikh, T., Thomas, D., Maraston, C., et al. 2018, *MNRAS*, **477**, 3954
- Pasquali, A., Gallazzi, A., & van den Bosch, F. C. 2012, *MNRAS*, **425**, 273
- Peoples, M. S., & Shankar, F. 2011, *MNRAS*, **417**, 2962
- Pellegrini, E. W., Reissl, S., Rahner, D., et al. 2019, arXiv:1905.04158
- Peng, Y., Maiolino, R., & Cochrane, R. 2015, *Natur*, **521**, 192
- Peng, Y.-j., Lilly, S. J., Renzini, A., & Carollo, M. 2012, *ApJ*, **757**, 4
- Peng, Y.-j., & Maiolino, R. 2014, *MNRAS*, **438**, 262
- Pettini, M., & Pagel, B. E. J. 2004, *MNRAS*, **348**, L59
- Poetrodjojo, H., Groves, B., Kewley, L. J., et al. 2018, *MNRAS*, **479**, 5235
- Prochaska, J. X., Werk, J. K., Worsack, G., et al. 2017, *ApJ*, **837**, 169
- Quirk, W. J., & Tinsley, B. M. 1973, *ApJ*, **179**, 69
- Renzini, A., & Andreon, S. 2014, *MNRAS*, **444**, 3581
- Robotham, A. S. G., Norberg, P., Driver, S. P., et al. 2011, *MNRAS*, **416**, 2640
- Rosales-Ortega, F. F., Sánchez, S. F., Iglesias-Páramo, J., et al. 2012, *ApJL*, **756**, L31
- Rubin, K. H. R., Prochaska, J. X., Koo, D. C., & Phillips, A. C. 2012, *ApJL*, **747**, L26
- Sánchez-Blázquez, P., Peletier, R. F., Jiménez-Vicente, J., et al. 2006, *MNRAS*, **371**, 703
- Sánchez, S. F., Kennicutt, R. C., Gil de Paz, A., et al. 2012, *A&A*, **538**, A8
- Schaefer, A. L., Croom, S. M., Scott, N., et al. 2019, *MNRAS*, **483**, 2851
- Smee, S. A., Gunn, J. E., Uomoto, A., et al. 2013, *AJ*, **146**, 32
- Smirnov, N. V. 1939, *Bull. Math. Univ. Moscou*, **2**, 3
- Tempel, E., Tuvikene, T., Kipper, R., & Libeskind, N. I. 2017, *A&A*, **602**, A100

- Tremonti, C. A., Heckman, T. M., Kauffmann, G., et al. 2004, *ApJ*, **613**, 898
- Trussler, J., Maiolino, R., Maraston, C., et al. 2018, arXiv:1811.09283
- Vincenzo, F., Matteucci, F., Belfiore, F., & Maiolino, R. 2016, *MNRAS*, **455**, 4183
- von der Linden, A., Wild, V., Kauffmann, G., White, S. D. M., & Weinmann, S. 2010, *MNRAS*, **404**, 1231
- Wake, D. A., Bundy, K., Diamond-Stanic, A. M., et al. 2017, *AJ*, **154**, 86
- Westfall, K. B., Cappellari, M., Bershady, M. A., et al. 2019, arXiv:1901.00856
- Wu, P.-F., Zahid, H. J., Hwang, H. S., & Geller, M. J. 2017, *MNRAS*, **468**, 1881
- Wuyts, S., Förster Schreiber, N. M., van der Wel, A., et al. 2011, *ApJ*, **742**, 96
- Yan, R., Bundy, K., Law, D. R., et al. 2016, *AJ*, **152**, 197
- Yuan, T. T., Kewley, L. J., & Richard, J. 2013, *ApJ*, **763**, 9
- Zahid, H. J., Dima, G. I., Kewley, L. J., Erb, D. K., & Davé, R. 2012, *ApJ*, **757**, 54
- Zhu, G. B., Barrera-Ballesteros, J. K., Heckman, T. M., et al. 2017, *MNRAS*, **468**, 4494